Thermal and Environmental Stability of Semi-Transparent Perovskite Solar Cells for Tandems Enabled by a Solution-Processed Nanoparticle Buffer Layer and Sputtered ITO Electrode

Kevin A. Bush, Colin D. Bailie, Ye Chen, Andrea R. Bowring, Wei Wang, Wen Ma, Tomas Leijtens, Farhad Moghadam, and Michael D. McGehee*

Metal–halide perovskite solar cells have reached 20% efficiency,[1] generating substantial interest in the technology. Solution-processability, compatibility with large-area deposition techniques, inexpensive input materials, desirable material properties such as bandgap tunability,[2] high open-circuit voltage (V_{OC}),[3] long ambipolar diffusion lengths,[4] and strong absorption[5] make this material very attractive for solar energy. Tandems of perovskites on top of silicon (Si) or copper indium gallium diselenide (CIGS) cells are considered a pathway to achieving industry goals of improving efficiency while lowering costs.[6–17]

Environmental stability[18] remains a key challenge to the commercialization of perovskite solar cells. The perovskite is susceptible to moisture ingress,[2,19] methylammonium iodide (MAI) egress,[20] and corrosion of metal electrodes by reaction with halides in the perovskite.[21] Early work has been performed on stabilizing the perovskite, including using hydrophobic heterojunction contacts or an additional encapsulation layer to prevent moisture ingress[18,22,23] or a pinhole-free metal oxide layer to prevent metal–halide interaction.[24] However, the need remains to find a holistic solution for all three main degradation routes. Here, we show that indium tin oxide (ITO), which has good moisture barrier properties,[25] also prevents the egress of the methylammonium iodide with evidence that the corrosion of the metal electrode is stopped as well. ITO and potentially other oxide layers greatly slow down or completely prevent three of the fastest degradation mechanisms in perovskite devices.

A highly transparent and conductive electrode is essential to the functionality of perovskite tandem solar cells. We have previously used silver nanowires (AgNWs),[8,12] but the formation of AgI significantly hinders stability[21] as 2,2′,7,7′-tetrakis(*N,N*-di-*p*-methoxyphenylamine)-9,9′-spirobifluorene (spiro-OMeTAD)

is an imperfect diffusion barrier for iodide. Others have used amorphous indium zinc oxide (IZO),[16] amorphous aluminum-doped zinc oxide (AZO),[10] Ni mesh,[26] graphene,[11] and thin metal layers.[6,14] However, the industry standard transparent conducting oxide (TCO) is ITO, which has the lowest resistivity of commercial TCOs and broadband transparency.[27] Thin films of ITO are typically deposited commercially through magnetron sputtering. In devices with soft materials such as the perovskite, the high energy sputtered particles and high temperatures during deposition and post annealing may accelerate methylammonium iodide evolution and result in irreversible damage of the perovskite active layer and the organic carrier extraction layers.[28,29]

It is currently impractical to deposit ITO directly onto the perovskite and carrier extraction layers due to this damage. Previous reports of sputtering a TCO onto the perovskite have used MoO$_X$ as a buffer layer between the active layers and the TCO.[7,10,16] The MoO$_X$ buffer layer has been implemented with limited success, generally reducing the fill factor (FF) and sometimes the open-circuit voltage compared to metal-electrode counterparts. The long-term stability of this buffer layer solution is uncertain, with evidence that the iodide in the perovskite can chemically react with the MoO$_X$ and form an extraction barrier.[30] Furthermore, thermal evaporation of a buffer layer is only feasible for hole-selective oxide layers such as MoO$_X$ and V$_2$O$_5$ that are deposited at low temperature and do not require a post anneal. For electron-selective layers such as TiO$_2$[31] or ZnO,[32] thermal evaporation of these layers requires high temperatures during deposition, post annealing, and often forms rough surfaces or nanowires rather than planar surfaces.

We demonstrate the use of solution-processed oxide nanoparticles as a simple and effective hole-blocking layer and sputtering buffer layer enabling ITO deposition without degradation of the layers underneath. We achieve a semi-transparent perovskite solar cell with an inverted architecture that we mechanically stack onto a silicon solar cell in a tandem configuration. We demonstrate perovskite device stability at 35 and 100 °C in ambient atmosphere under one-sun equivalent visible illumination at the maximum power point, and extract the temperature coefficient of efficiency for our semi-transparent perovskite device. The stability of the solar cells at 100 °C demonstrates that previous concerns over methylammonium iodide egress and thermal and environmental instability of CH$_3$NH$_3$PbI$_3$ perovskite solar cells may be mitigated by inclusion of a simple barrier layer.

K. A. Bush, Dr. C. D. Bailie, A. R. Bowring,
Dr. T. Leijtens, Prof. M. D. McGehee
Department of Materials Science
Stanford University
Lomita Mall, Stanford, CA, USA
E-mail: mmcgehee@stanford.edu
Dr. Y. Chen, Dr. W. Wang, Dr. W. Ma, Dr. F. Moghadam
SunPreme
Palomar Avenue, Sunnyvale, CA, USA
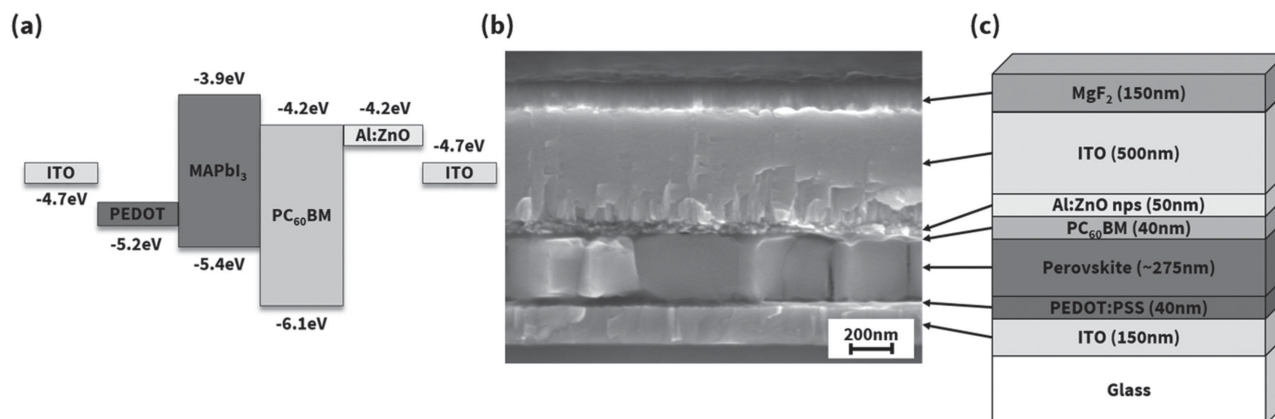
Figure 1. Semi-transparent inverted perovskite device architecture. a) Energy level diagram. Energy levels are selected from relevant literature values and product specifications. Values on bands represent valence and conduction band levels, while single values represent the work functions of those materials. b,c) Cross-sectional SEM and illustrative schematic of the device architecture showing the ITO electrode encapsulation layer.

Inverted perovskite solar cells, in which the perovskite is fabricated on top of a hole-selective contact, can achieve a high power conversion efficiency >18%.[33] Briefly, we spin poly(3,4-ethylenedioxythiophene) polystyrene sulfonate (PEDOT:PSS) onto ITO-coated glass for a smooth, hydrophilic *p*-type heterojunction layer. The perovskite is then deposited using a technique developed by Zhang et al.[34] followed by phenyl-C61-butyric acid methyl ester (PCBM) as an *n*-type heterojunction layer (see the Experimental Section for more details). We solution-deposit nanoparticles of the wide bandgap semiconductor ZnO to serve as an electron-selective buffer layer on top of the PCBM. The ZnO layer protects the underlying organic PCBM and perovskite layers from the sputter deposition process of the TCO. The large bandgap and well-aligned work function of ZnO to the perovskite enables its use as a selective contact (**Figure 1**a). Energy levels are selected from relevant literature values and product specifications.[24,35] ZnO has been demonstrated by Guo et al.[36] and was later shown by You et al.[24] to favorably affect the ambient stability of a perovskite solar cell. A 50 nm layer of ZnO nanoparticles (ZnO np) on the PCBM layer and an Al rear electrode enables a stabilized power output of 13.5% (**Figure 2**b).

We sputter 500 nm of ITO directly onto the ZnO np capped films to achieve a low sheet resistance of $\approx$9.9 Ω $\square^{-1}$ after annealing at 100 °C. The sputtering is performed by DC magnetron sputtering using a commercial grade 90:10 In_2O_3:SnO_2 wt.% ITO ceramic target (see Supporting Information for further details). Sputtering gases of Ar (4 sccm) and O_2 (0.3 sccm) with purity >99.995% are introduced into the chamber during deposition, which is performed at room temperature with a target power of 400 W (12 nm min^{-1} deposition rate). The transmission spectrum of identically processed ITO on a glass slide is shown in the Supporting Information. Figure 1b shows an SEM cross-section of the ITO electrode on top of the perovskite. The V_{OC} of these devices is greater than 0.9 V, indicating that ZnO successfully acts as a buffer layer to prevent sputter damage of the organic PCBM layer. However, a large interfacial barrier exists between the ZnO and ITO layers, preventing carrier extraction. This barrier is temporarily removed when operating the device at an elevated temperature of 70 °C, as shown in Figure 1 in the Supporting Information, but the barrier returns as the device cools. We speculate that the barrier arises from the misaligned work functions of ZnO and ITO. We introduce aluminum doped (2 mol%) zinc oxide (AZO) nanoparticles to
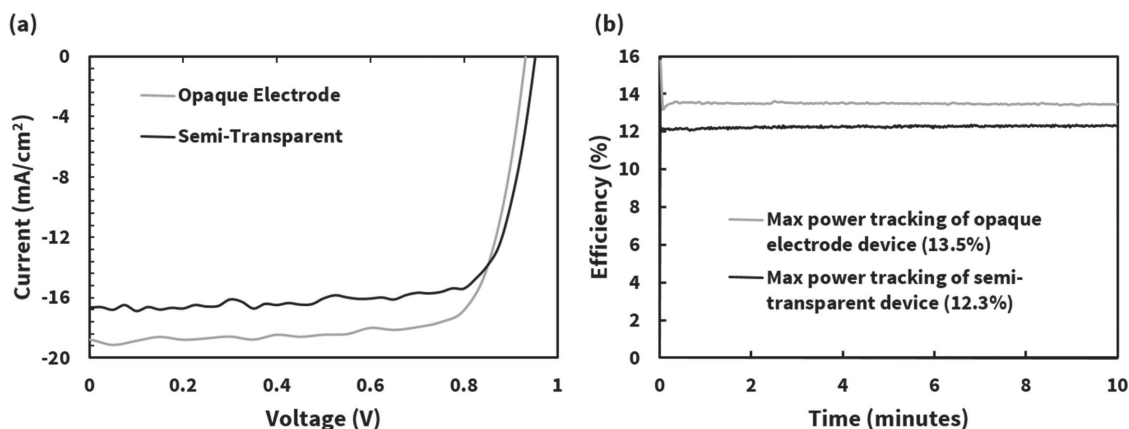
Figure 2. Performance comparison of the opaque and semi-transparent devices showing (a) the *J*–*V* curve of devices showing comparable FF and V_{OC} and (b) the maximum power point of tracking. The early time transient is not included in the steady-state power determination.

Table 1. Photovoltaic parameters of a semi-transparent perovskite solar cell with an ITO rear electrode compared to an opaque perovskite solar cell with an Al/Ag rear electrode.

	J_{SC}[a] [mA cm^{-2}]	V_{OC} [mV]	FF [–]	η[b] [%]
Opaque	18.8	938	0.77	13.5
Semi-transparent	16.5	952	0.77	12.3

[a]Obtained from EQE integration of AM1.5G spectrum; [b]obtained from maximum power point tracking.

eliminate the extraction barrier, allowing the device to operate optimally at 25 °C.

Anti-reflection coatings are applied to both air interfaces for peak performance. 105 nm of MgF$_2$ is deposited by thermal evaporation onto the glass surface and 150 nm of MgF$_2$ is deposited onto the ITO surface. These thicknesses are chosen based on transfer matrix modeling of the thin film stack. Simply, 105 nm is deposited onto the glass surface to provide anti-reflection primarily for wavelengths relevant to the perovskite ($\lambda/4n = t$ implies anti-reflection centered around 580 nm) and 150 nm is deposited onto the ITO surface to provide anti-reflection primarily for wavelengths relevant to the silicon ($\lambda/4n = t$ implies anti-reflection centered around 825 nm).

The current-voltage (J–V) curves of the opaque (Al/Ag electrode) and semi-transparent (ITO electrode) devices are shown in Figure 2a. The AZO nanoparticles allow operation of the semi-transparent device at room temperature with a stabilized power efficiency of 12.3% (Figure 2b). The semi-transparent device displays a high fill factor of 0.77 with a V_{OC} of 0.95 V and short-circuit current density (J_{SC}) of 16.5 mA cm^{-2} (Table 1). In Figure 7 in the Supporting Information, we show that devices without any buffer layer (6% efficient) or with an organic buffer layer (8% efficient) instead of AZO perform substantially worse, likely due to damage to the organic layer and perovskite during sputtering. The semi-transparent device with a top electrode area of 6 mm × 11 mm is illuminated through a 4.5 mm × 8.75 mm aperture mask and the opaque device with a top electrode area of 4 mm × 5 mm is illuminated through a 3 mm × 4 mm aperture mask. We scan the devices in a positive to negative voltage direction with a step size of 50 mV and a delay time between points of 0.2 s. The adequate performance of the sputtered ITO electrode is confirmed by the comparable FF and voltage in the opaque and semi-transparent devices. The drop in current density in the semi-transparent device can be explained by the lack of a metal electrode back-reflector to increase light absorption. This decrease primarily occurs at longer wavelengths as shown by the external quantum efficiency (EQE) spectrum in Figure 4 in the Supporting Information.

Recent work has demonstrated that exposure to moisture results in the formation of both mono- and di-hydrates of the CH$_3$NH$_3$PbI$_3$ material, which slowly degrades into PbI$_2$.[37–39] This process is accelerated by heat, which induces egress of methylammonium iodide, and electric fields, which induce drift of methylammonium and iodide.[18] It is crucial to exclude water from reaching the perovskite layer. Other recent work has suggested that the material is thermally unstable even in inert conditions, and that heating to just 85 °C in a nitrogen atmosphere results in methylammonium iodide decomposition and egress.[20]

To start our studies on the stability of semi-transparent devices with an amorphous ITO capping layer, we operate opaque and semi-transparent cells at the maximum power point under one-sun equivalent visible illumination at 35 and 100 °C in an ambient atmosphere without additional encapsulation (**Figure 3**). The perovskite is capped with PCBM then AZO nanoparticles followed by either Al/Ag (opaque) or ITO (semi-transparent). The opaque device has a structure similar to the recently published study by You et al.[24] that demonstrated improved ambient stability stored in the dark compared to devices without a nanoparticle layer. The semi-transparent devices are illuminated through the 500 nm thick sputtered ITO layer during these tests. To avoid convolution of the role of ITO in stabilizing the perovskite, these devices do not have MgF$_2$ anti-reflection coatings on top of the ITO. As shown in Figure 4 in the Supporting Information, this ITO layer acts as an effective UV filter, so we do not expect a difference in degradation profile when illuminated with a full spectrum light source.

At both 35 and 100 °C, we observe rapid degradation of the opaque cells and find that the nanoparticle layer is an insufficient barrier to prevent degradation, despite its reported effectiveness as a moisture barrier. This result agrees with Conings et al.[20] suggesting that the methylammonium iodide evolves as a gas (likely as CH$_3$NH$_2$ and HI), leaving behind PbI$_2$ (see Figure 3c,d and video in the Supporting Information). It is likely that HI corrodes the metal electrode. We perform X-ray diffraction (XRD) on metal-electrode devices both before and after operating the device at 100 °C under illumination for 1.3 h (Figure 3c), which is the time to reach 9% of initial efficiency for the metal-electrode device as shown in Figure 3b. We observe partial conversion of the perovskite into PbI$_2$. The results make it clear that storage (in dark conditions) or operation at room temperature is an insufficient metric to represent the stability of devices operated in the field; exposure to increased temperatures under illumination is necessary to fully evaluate layers used to improve the stability of perovskite cells.

The device capped with an ITO layer required 124 h to reach 80% of its original efficiency (T_{80}) when operated at 100 °C (see Figure 11 in the Supporting Information for data on a second device which lasted 138 h), compared to metal electrode devices with a T_{80} of 1 h at 35 °C and 1.5 min at 100 °C. We are unable to extract a T_{80} lifetime of the 35 °C ITO-capped device within the scope of this study. We perform X-ray diffraction experiments before and after operating the semi-transparent device at 100 °C under illumination for 1.3 h. We observe no change in the XRD spectrum. Because the semi-transparent cells have not changed in the XRD spectrum on this timescale while the opaque cells have, we posit that the ITO capping layer has prevented the egress of methylammonium iodide, effectively sealing in the perovskite. We note that there is strong evidence from the literature that the ITO layer has also prevented moisture ingress[2,27] as well as prevented halide corrosion of the metal electrode,[21] though direct proof is beyond the scope of this work (see Figure 3d and the video in the Supporting Information for visual evidence of the sealing effect). We speculate that the initial improvement we see in device performance over the first 10–20 h of device operation may be due to ion migration and potentially chemical doping of the PCBM layer

COMMUNICATION
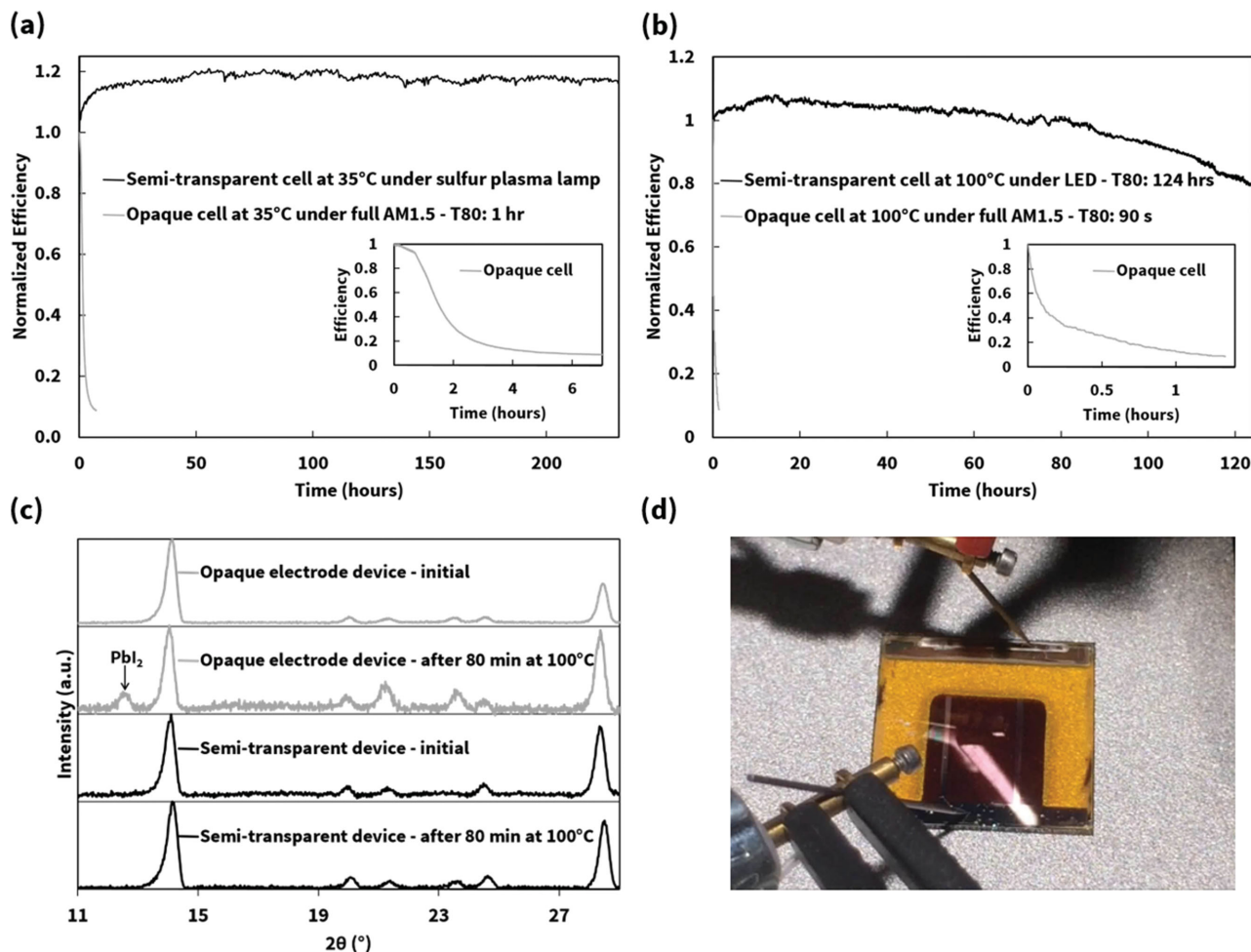
Figure 3. Thermal stability of ITO-capped perovskite solar cells at (a) 35 °C and (b) 100 °C compared to the opaque device with AZO and Al/Ag. c) XRD data of opaque electrode and semi-transparent devices before and after testing for 80 min at 100 °C under illumination. A PbI_2 peak arises in the opaque electrode device, while no such change occurs in the semi-transparent device. d) A semi-transparent perovskite solar cell operated at 150 °C under illumination. Photo taken after 90 s. The ITO layer is only in the middle, clearly showing the degradation of the perovskite on the uncovered areas around the ITO into PbI_2 (see also the video in the Supporting Information).

by iodide[40] as well as crystallization of the ITO, improving its optoelectronic properties. We hypothesize that the slow degradation over time is due to the lack of an edge seal on the solar cell, allowing lateral diffusion and escape of methylammonium iodide as well as ingress of moisture. We expect further sealing of the cell to mitigate these open pathways for degradation. The slow degradation of device performance is also strong support for the notion that the ionic motion responsible for hysteresis does not necessarily induce degradation in operating devices as long as they are well encapsulated.[18,22] Additionally, we note the organic charge extraction layers are protected by the ITO electrode barrier.

In addition to improved thermal stability, we extract efficiency values at multiple temperatures to estimate the efficiency temperature coefficient of the semi-transparent solar cell (Figure 10, Supporting Information). We measure the temperature coefficient as −0.22% (rel)/°C (**Table 2**), a significant improvement over the −0.34% (rel)/°C for a commercial CdTe module.[41]

We test our semi-transparent device in a mechanically stacked tandem configuration with a monocrystalline silicon

(mono-Si) bottom cell. In this laboratory-scale experiment, the tandem is tested in a 4-terminal configuration, meaning that the top and bottom cells are stacked on top of one another (optically coupled) but are measured separately for their performance (electrically decoupled). We note that at the module level, such mechanically stacked tandems can be wired into 2-terminal configurations if the size of the cells is chosen to enable current or voltage matching.[42] The results are summarized in

Table 2. Efficiency as a function of temperature extracted by averaging the data in Figure 10 in the Supporting Information over the entire time period. The temperature coefficient is extracted as a linear fit of the data and normalized against the expected efficiency at 25 °C.

Temperature [°C]	Efficiency [%]
35	12.20
60	11.67
100	10.46
Temperature coefficient	−0.22% (rel)/°C

© 2016 WILEY-VCH Verlag GmbH & Co. KGaA, Weinheim
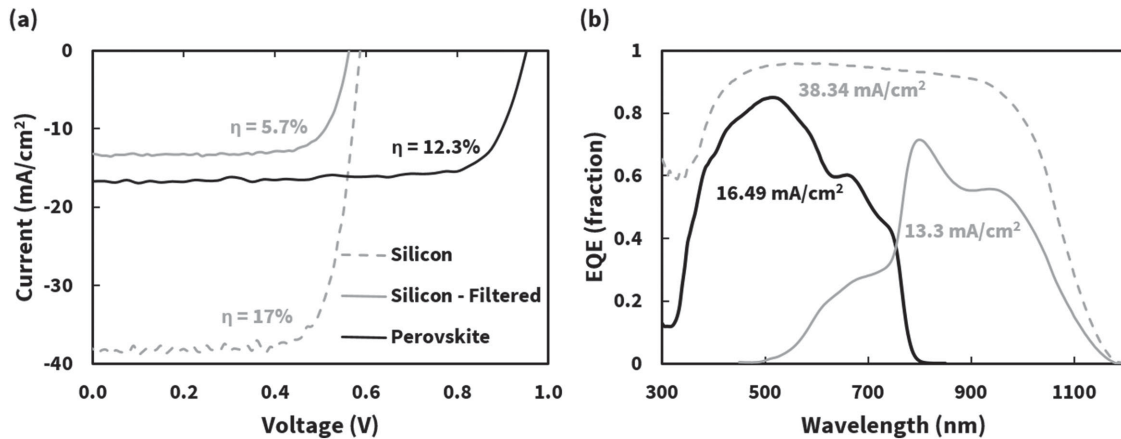
Figure 4. Mechanically stacked perovskite/silicon tandem performance. a) J–V curves of tandem with the maximum power of the tandem calculated from the addition of the perovskite and silicon cells. b) External quantum efficiency of original mono-Si, perovskite, and filtered silicon solar cells.

Figure 4 and **Table 3**. Alone, the efficiency of the mono-Si is 17.0%. The silicon cell (6 mm × 13 mm) is limited in V_{OC} due to excess shaded area from the aperture mask and the top electrode. With the semi-transparent perovskite solar cell stacked in front of the mono-Si cell, the efficiency improves to 18.0% in a tandem (12.3% + 5.7%) with a J_{SC} of 13.3 mA cm^{-2} from the filtered Si bottom cell. Strong coherent reflections (see Figure 6 in the Supporting Information) limit the transmission through the perovskite cell and the J_{SC} of the filtered silicon cell.

In this initial demonstration, although we have not yet tested a large enough sample set of devices at 35 or 100 °C to state a T_{80} lifetime with statistical certainty, we have shown that using an ITO top electrode overcomes the catastrophic degradation observed in unencapsulated devices with a metal electrode that has so far prevented the investigation of the long-term degradation mechanisms in the perovskite. We plan to measure the lifetime of a large collection of fully encapsulated solar cells at a variety of temperatures to determine the acceleration factor for degradation and the T_{80} at room temperature. The initial results here lead us to expect that determining confidence in a room temperature T_{80} value will require at least 6 months of continuous operation under light.

These ITO-coated devices are now in the thermal and ambient stability range required to be transported in air and further encapsulated in transparent crosslinkable polymers and glass during volume manufacturing processes that are necessary to enable operational lifetimes extending to 25 years and beyond. This simplifies the air purification requirements

during manufacturing and allows for the use of traditional photovoltaic encapsulants that are typically laminated at temperatures above 100 °C. The semi-transparent cell and mechanically stacked tandem with ITO top electrodes demonstrate a path towards stable and efficient single-junction perovskite and perovskite/silicon tandem solar cells.

Experimental Section

Perovskite Device Fabrication: 10 Ω □$^{-1}$ ITO-coated glass (Xin Yan Technology), coated with 105 nm of MgF$_2$ on the reverse side was coated with Al 4083 PEDOT:PSS (Clevios) at 4000 rpm for 30 s and dried at 135 °C for 15 min. A 40 wt.% solution was made of 3:1 molar ratio methylammonium iodide (Dyesol) to lead acetate (PbAc$_2$, Sigma) in anhydrous N,N-dimethylformamide (DMF, Acros) with 0.75% HPA/PbAc$_2$ hypophosphorous acid (HPA, Sigma Aldrich). The solution of MAI and PbAc$_2$ was spun at 2000 rpm for 60 s. The films were dried at room temperature and then annealed at 100 °C for 5 min in dry air. A 2 wt.% solution of PCBM (Solenne bv) in anhydrous DCB was spun at 3000 rpm for 45 s and annealed for 5 min at 90 °C. AZO (Sigma) or ZnO (Sigma) nanoparticle inks with 15 nm average particle diameter dispersed in IPA (2.5 wt.%) were spun on at 4000 rpm. Two layers of nanoparticles were spun sequentially to produce an approximately 50 nm thick layer. The ZnO and AZO films were dried at 75 °C for 5 min.

For the opaque devices, 100 nm of Al and 125 nm of Ag were thermally evaporated through a patterned shadow mask with a 0.2 cm^2 aperture size as the back electrode. An improvement in air stability was observed with the addition of the Ag layer.

For the semi-transparent devices, 500 nm of ITO was sputtered onto the device using a base pressure < 5 × 10^{-6} Torr, deposition pressure of 2 × 10^{-3}, a power density of 8 W in.$^{-2}$, and 5% oxygen partial pressure. The devices were post annealed at 100 °C for 15 min. 250 nm of Ag was evaporated around the perimeter of the device, leaving a 0.6 cm^2 aperture size open. Finally, 150 nm of MgF$_2$ was thermally evaporated as an anti-reflection coating.

J–V Measurements: Current–voltage measurements were performed using a Keithley model 2400 digital source meter and 300W xenon lamp (Oriel) solar simulator was used for irradiation. The lamp was calibrated against the integrated photocurrent calculated by EQE. J–V curves were taken from forward to reverse bias. Reported values for efficiency were obtained by operating the cells at steady-state maximum power and averaging over a minimum of 60 s. The opaque and semi-transparent cells were illuminated through a 0.12 and 0.39 cm^2 aperture area, respectively.

Table 3. Photovoltaic parameters of semi-transparent perovskite and mono-crystalline silicon cells and the resulting tandem efficiency.

	J_{SC} [mA cm^{-2}]	V_{OC} [mV]	FF [–]	η [%]
Perovskite	16.5	952	0.774	12.3[a]
Silicon	38.3	587	0.754	17.0
Filtered silicon	13.3	562	0.762	5.7
Mechanically stacked tandem				18.0

[a]Obtained from the maximum power point tracking.

EQE Measurements: EQE was recorded as a function of the wavelength using a Keithley model 236 without light bias. A 100 W tungsten lamp (Newport) was used to provide an excitation beam, which was focused through a Princeton Instruments SpectraPro 150 monochromator and chopped at approximately 0.6 Hz. At each wavelength, data was collected for and averaged for 5 s. To measure the EQE of the bottom cell in the tandem, the above procedure for the Si was repeated with the perovskite top cell placed in front of the Si or CIGS cell to filter the incoming light.

4-Point Probe and Transmission Measurements: Sheet resistance and transmission measurements were performed as previously described in the supplemental section of Beiley et al. (2013).[43]

Thermal Stability Measurements: To test the thermal stability of these devices, two different setups were used. For the 35 °C experiments, devices were placed under a sulfur plasma lamp. The sulfur plasma lamp was from LF (6000K blackbody), which had emission primarily in the visible spectrum. A ReflecTech Mirror film laminated on a plastic sheet into a conical reflector helped creating homogeneous light intensity. Science Wares Inc. customized electronics were used to control and monitor the solar cells at the maximum power point. The surface of the solar cell at steady-state during operation was measured at 35 °C with a surface temperature probe. For the 100 °C experiments, the devices were placed on a hotplate with a 100 °C surface. An Enfis white LED array was used as the light source and the maximum power point was monitored using a Keithley model 2400 digital source meter.

XRD Measurements: X-ray diffraction measurements were carried out in air on a Panalytical X'pert Pro Diffractometer with a Cu Kα source (wavelength of 1.5405 Å).

Supporting Information

Supporting Information is available from the Wiley Online Library or from the author.

Acknowledgements

[1] "NREL Efficiency Chart Rev. 08-06-2015," http://www.nrel.gov/ncpv/images/efficiency_chart.jpg, **2015**.

[2] J. H. Noh, S. H. Im, J. H. Heo, T. N. Mandal, S. Il Seok, *Nano Lett.* **2013**, *13*, 1764.

[3] J. P. Correa Baena, L. Steier, W. Tress, M. Saliba, S. Neutzner, T. Matsui, F. Giordano, T. J. Jacobsson, A. R. Srimath Kandada, S. M. Zakeeruddin, A. Petrozza, A. Abate, M. K. Nazeeruddin, M. Grätzel, A. Hagfeldt, *Energy Environ. Sci.* **2015**, *8*, 2928.

[4] S. D. Stranks, G. E. Eperon, G. Grancini, C. Menelaou, M. J. P. Alcocer, T. Leijtens, L. M. Herz, A. Petrozza, H. J. Snaith, *Science* **2013**, *342*, 341.

[5] P. Löper, M. Stuckelberger, B. Niesen, J. Werner, M. Filipič, S.-J. Moon, J.-H. Yum, M. Topič, S. De Wolf, C. Ballif, *J. Phys. Chem. Lett.* **2014**, *6*, 66.

[6] T. Todorov, T. Gershon, O. Gunawan, C. Sturdevant, S. Guha, *Appl. Phys. Lett.* **2014**, *105*, 173902.

[7] P. Löper, S.-J. Moon, S. Martín de Nicolas, B. Niesen, M. Ledinsky, S. Nicolay, J. Bailat, J.-H. Yum, S. De Wolf, C. Ballif, *Phys. Chem. Chem. Phys.* **2015**, *17*, 1619.

[8] C. D. Bailie, M. G. Christoforo, J. P. Mailoa, A. R. Bowring, E. L. Unger, W. H. Nguyen, J. Burschka, N. Pellet, J. Z. Lee, M. Grätzel, R. Noufi, T. Buonassisi, A. Salleo, M. D. McGehee, *Energy Environ. Sci.* **2015**, *8*, 956.

[9] C. D. Bailie, M. D. McGehee, *MRS Bull.* **2015**, *40*, 681.

[10] L. Kranz, A. Abate, T. Feurer, F. Fu, E. Avancini, J. Löckinger, P. Reinhard, S. M. Zakeeruddin, M. Grätzel, S. Buecheler, A. N. Tiwari, *J. Phys. Chem. Lett.* **2015**, *6*, 2676.

[11] F. Lang, M. a. Gluba, S. Albrecht, J. Rappich, L. Korte, B. Rech, N. H. Nickel, *J. Phys. Chem. Lett.* **2015**, *6*, 2745.

[12] J. P. Mailoa, C. D. Bailie, E. C. Johlin, E. T. Hoke, A. J. Akey, W. H. Nguyen, M. D. McGehee, T. Buonassisi, *Appl. Phys. Lett.* **2015**, *106*, 121105.

[13] R. Sheng, A. W. Y. Ho-Baillie, S. Huang, M. Keevers, X. Hao, L. Jiang, Y.-B. Cheng, M. a. Green, *J. Phys. Chem. Lett.* **2015**, *6*, 3931.

[14] T. Todorov, T. Gershon, O. Gunawan, Y. S. Lee, C. Sturdevant, L.-Y. Chang, S. Guha, *Adv. Energy Mater.* **2015**, *5*, DOI: 10.1002/aenm.201500799.

[15] H. Uzu, M. Ichikawa, M. Hino, K. Nakano, T. Meguro, J. L. Hernández, H.-S. Kim, N.-G. Park, K. Yamamoto, *Appl. Phys. Lett.* **2015**, *106*, 013506.

[16] J. Werner, G. Dubuis, A. Walter, P. Löper, S. Moon, S. Nicolay, M. Morales-masis, S. De Wolf, B. Niesen, C. Ballif, **2015**, *141*, 407.

[17] Y. M. Yang, Q. Chen, Y. Hsieh, T. Song, N. De Marco, H. Zhou, Y. Yang, *ACS Nano* **2015**, *9*, 7714.

[18] T. Leijtens, G. E. Eperon, N. K. Noel, S. N. Habisreutinger, A. Petrozza, H. J. Snaith, *Adv. Energy Mater.* **2015**, *5*, DOI: 10.1002/aenm.201500963.

[19] S. N. Habisreutinger, T. Leijtens, G. E. Eperon, S. D. Stranks, R. J. Nicholas, H. J. Snaith, *Nano Lett.* **2014**, *14*, 5561.

[20] B. Conings, J. Drijkoningen, N. Gauquelin, A. Babayigit, J. D'Haen, L. D'Olieslaeger, A. Ethirajan, J. Verbeeck, J. Manca, E. Mosconi, F. De Angelis, H.-G. Boyen, *Adv. Energy Mater.* **2015**, *5*, DOI: 10.1002/aenm.201500477.

[21] Y. Kato, L. K. Ono, M. V. Lee, S. Wang, S. R. Raga, Y. Qi, *Adv. Mater. Interfaces* **2015**, *2*, DOI: 10.1002/admi.201500195.

[22] X. Li, M. Tschumi, H. Han, S. S. Babkair, R. A. Alzubaydi, A. A. Ansari, S. S. Habib, M. K. Nazeeruddin, S. M. Zakeeruddin, M. Grätzel, *Energy Technol.* **2015**, *3*, 551.

[23] A. Mei, X. Li, L. Liu, Z. Ku, T. Liu, Y. Rong, M. Xu, M. Hu, J. Chen, Y. Yang, M. Grätzel, H. Han, *Science* **2014**, *345*, 295.

[24] J. You, L. Meng, T.-B. Song, T.-F. Guo, Y. (Michael) Yang, W.-H. Chang, Z. Hong, H. Chen, H. Zhou, Q. Chen, Y. Liu, N. De Marco, Y. Yang, *Nat. Nanotechnol.* **2015**, *11*, 75.

[25] B. M. Henry, A. G. Erlat, A. McGuigan, C. R. M. Grovenor, G. A. D. Briggs, Y. Tsukahara, T. Miyamoto, N. Noguchi, T. Niijima, *Thin Solid Films* **2001**, *382*, 194.

[26] D. Bryant, P. Greenwood, J. Troughton, M. Wijdekop, M. Carnie, M. Davies, K. Wojciechowski, H. J. Snaith, T. Watson, D. Worsley, *Adv. Mater.* **2014**, *26*, 7499.

[27] K. Ellmer, *Nat. Photonics* **2012**, *6*, 808.

[28] J. Meyer, S. Hamwi, M. Kröger, W. Kowalsky, T. Riedl, A. Kahn, *Adv. Mater.* **2012**, *24*, 5408.

Materials Views
www.MaterialsViews.com

ADVANCED
MATERIALS
www.advmat.de

COMMUNICATION

[29] L. S. Liao, L. S. Hung, W. C. Chan, X. M. Ding, T. K. Sham, I. Bello, C. S. Lee, S. T. Lee, *Appl. Phys. Lett.* **1999**, *75*, 1619.

[30] P. Liu, X. Liu, L. Lyu, H. Xie, H. Zhang, D. Niu, H. Huang, C. Bi, Z. Xiao, J. Huang, Y. Gao, *Appl. Phys. Lett.* **2015**, *106*, 193903.

[31] A. MortezaAli, S. Sani, *J. Nanostruct. Chem.* **2013**, *3*, 35.

[32] O. Fouad, A. Ismail, Z. Zaki, R. Mohamed, *Appl. Catal. B* **2006**, *62*, 144.

[33] C. Bi, Q. Wang, Y. Shao, Y. Yuan, Z. Xiao, J. Huang, *Nat. Commun.* **2015**, *6*, 7747.

[34] W. Zhang, M. Saliba, D. T. Moore, S. K. Pathak, M. T. Hörantner, T. Stergiopoulos, S. D. Stranks, G. E. Eperon, J. a. Alexander-Webber, A. Abate, A. Sadhanala, S. Yao, Y. Chen, R. H. Friend, L. a. Estroff, U. Wiesner, H. J. Snaith, *Nat. Commun.* **2015**, *6*, 6142.

[35] W. Chen, Y. Wu, Y. Yue, J. Liu, W. Zhang, X. Yang, H. Chen, E. Bi, I. Ashraful, M. Grätzel, L. Han, *Science* **2015**, *350*, 944.

[36] F. Guo, H. Azimi, Y. Hou, T. Przybilla, M. Hu, C. Bronnbauer, S. Langner, E. Spiecker, K. Forberich, C. J. Brabec, *Nanoscale* **2015**, *7*, 1642.

[37] J. Yang, B. D. Siempelkamp, D. Liu, T. L. Kelly, *ACS Nano* **2015**, *9*, 1955.

[38] J. A. Christians, P. A. Miranda Herrera, P. V. Kamat, *J. Am. Chem. Soc.* **2015**, *137*, 1530.

[39] A. M. A. Leguy, Y. Hu, M. Campoy-Quiles, M. I. Alonso, O. J. Weber, P. Azarhoosh, M. van Schilfgaarde, M. T. Weller, T. Bein, J. Nelson, P. Docampo, P. R. F. Barnes, *Chem. Mater.* **2015**, *27*, 3397.

[40] M. De Bastiani, G. Dell'Erba, M. Gandini, V. D'Innocenzo, S. Neutzner, A. R. S. Kandada, G. Grancini, M. Binda, M. Prato, J. M. Ball, M. Caironi, A. Petrozza, *Adv. Energy Mater.* **2015**.

[41] First Solar Series 4 PV Module Datasheet, **2015**.

[42] C. D. Bailie, M. G. Christoforo, J. P. Mailoa, A. R. Bowring, E. L. Unger, W. H. Nguyen, J. Burschka, N. Pellet, J. Z. Lee, M. Grätzel, R. Noufi, T. Buonassisi, A. Salleo, M. D. McGehee, *Energy Environ. Sci.* **2015**, *8*, 956.

[43] Z. M. Beiley, M. G. Christoforo, P. Gratia, A. R. Bowring, P. Eberspacher, G. Y. Margulis, C. Cabanetos, P. M. Beaujuge, A. Salleo, M. D. McGehee, *Adv. Mater.* **2013**, *25*, 7020.